Cusp dynamics under northward IMF using three-dimensional global particle-in-cell simulations

Dongsheng Cai, Amin Esmaeili, Bertrand Lembège, Ken-Ichi Nishikawa

▶ **To cite this version:**

Dongsheng Cai, Amin Esmaeili, Bertrand Lembège, Ken-Ichi Nishikawa. Cusp dynamics under northward IMF using three-dimensional global particle-in-cell simulations. Journal of Geophysical Research Space Physics, American Geophysical Union/Wiley, 2015, 120 (10), pp.8368-8386. 10.1002/2015JA021230 . insu-01231973

HAL Id: insu-01231973

https://hal-insu.archives-ouvertes.fr/insu-01231973

Submitted on 8 Sep 2020

HAL is a multi-disciplinary open access archive for the deposit and dissemination of scientific research documents, whether they are published or not. The documents may come from teaching and research institutions in France or abroad, or from public or private research centers.

L'archive ouverte pluridisciplinaire **HAL**, est destinée au dépôt et à la diffusion de documents scientifiques de niveau recherche, publiés ou non, émanant des établissements d'enseignement et de recherche français ou étrangers, des laboratoires publics ou privés.

AGU PUBLICATIONS

JGR

Journal of Geophysical Research: Space Physics

RESEARCH ARTICLE
10.1002/2015JA021230

Key Points:
- The interaction of the solar wind with the magnetosphere is simulated
- The simulation results are compared with MHD and Cluster data
- The exterior cusp identified in Cluster data is retrieved

Correspondence to:
D. Cai,
dongscai@gmail.com

Citation:
Cai, D., A. Esmaeili, B. Lembège, and K.-I. Nishikawa (2015), Cusp dynamics under northward IMF using three-dimensional global particle-in-cell simulations, *J. Geophys. Res. Space Physics*, *120*, 8368–8386, doi:10.1002/2015JA021230.

Received 27 MAR 2015
Accepted 19 AUG 2015
Accepted article online 22 AUG 2015
Published online 7 OCT 2015

©2015. American Geophysical Union. All Rights Reserved.

Cusp dynamics under northward IMF using three-dimensional global particle-in-cell simulations

D. Cai[1], A. Esmaeili[1], B. Lembège[2], and K-I Nishikawa[3]

[1]Univeristy of Tsukuba, Tsukuba, Japan, [2]LATMOS - UVSQ - CNRS, Guyancourt, France, [3]National Space Science and Technology Center, Huntsville, Alabama, USA

Abstract The interaction of the solar wind with the terrestrial magnetosphere is analyzed with the help of three-dimensional (3-D) global, full-electromagnetic particle-in-cell (PIC) simulations, in the configuration where the interplanetary magnetic field (IMF) is steadily northward. The present study is mainly focused on the cusp region and associated particle momenta dynamics. Within the present context and to the best of our knowledge, this work represents the first numerical simulation for analyzing the cusp dynamics using a fully self-consistent 3-D kinetic and electromagnetic approach. The main goals of the study are the following: (i) to retrieve the main known features of the cusp to validate the use of 3-D PIC "global" simulations, (ii) to compare with previous results obtained with 3-D MHD simulations, (iii) to create an updated global view of the cusp based on use of 3-D PIC simulation, which cannot be obtained from a MHD approach, and (iv) to compare with statistical results from the Cluster mission. In particular, the stagnant exterior cusp (SEC) identified in previous statistical analysis of experimental data is retrieved, and it is possible to more precisely define the edges of the SEC region. In addition, we will focus on cusp features recently observed by the Cluster mission, for example, the Alfvén Transition Layer or ATL and on the features not reproduced by either MHD or the hybrid approach, which have been used to characterize the outer edges of the cusp more clearly.

1. Introduction

The early magnetospheric model by *Chapman and Ferraro* [1930] is the first to feature the magnetospheric cusp. The authors predicted that magnetosheath plasma might enter the magnetosphere through the null points at the poles of each hemisphere. Particles that enter this region may be energized and become the source for the plasma sheet. It is well known that the shape and dynamics of the magnetospheric cusp are strongly dependent on interplanetary magnetic field (IMF) orientation [*Lavraud et al.,* 2004, 2005]. In order to successfully model these features, it is critical to treat the interaction between the solar wind and terrestrial magnetosphere in its global context.

A global MHD simulation can properly simulate the transport of energy and momenta between different magnetospheric plasma regions, including the scales of the concerned regions, the general shape of the magnetosphere, and dependence on solar wind conditions [*Ogino et al.,* 1992; *Palmroth et al.,* 2003]. In spite of this success, open questions persist perhaps due to the presence of kinetic processes such as (1) the precipitation and acceleration of ions and electrons in the magnetic cusp region and (2) the transport of particles from the magnetic cusp to the plasma sheet. A more complete treatment of cusp dynamics is our objective for performing the 3-D global electromagnetic full PIC simulation described herein.

Large-scale global three-dimensional particle-in-cell (PIC) simulations are used here to analyze the interaction between the solar wind and the whole terrestrial magnetosphere. To our knowledge, this study is the first using a global 3-D PIC approach with a spatial resolution that can include the space charge effect. We first validate the ability to reproduce the basic known features of magnetospheric dynamics by comparison with previous 3-D MHD results and with a statistical characterization obtained from Cluster for northward IMF [*Lavraud et al.,* 2002, 2004, 2005]. We next focus on the simulation derived spatial features of the polar magnetic cusp region (in particular its boundaries) and on the associated particle momenta dynamics for northward IMF (to explore the kinetic effects). The simulations reported here are performed at a grid resolution of 0.2 Earth radii, at least 2.5 times smaller than that in previous works [*Cai et al.,* 2001, 2006a, 2006b, 2009; *Cai and Buneman*, 1992 etc.]. The strength of previous global 3D PIC simulations have been to analyze large scale patterns and processes such as magnetic sash formations [*Cai et al.,* 2006a, 2006b], 3-D magnetic field topologies, and bifurcation of terrestrial magnetospheric magnetic field [*Cai et al.,* 2001, 2006a, 2006b, 2009].

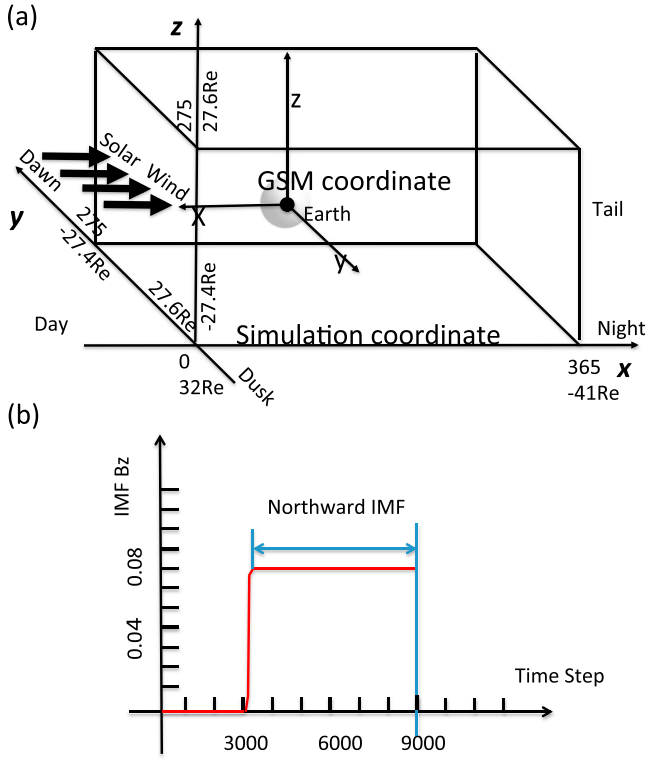

Figure 1. (a) Simulation reference frame and GSM (geocentric solar magnetospheric) frame; the Earth's center is located at (160Δ, 137Δ, 137Δ) where Δ is the unit space grid, or (32 R_E, 27.4 R_E, 27.4 R_E) in the simulation frame. In the simulation coordinate set, the left front corner is the origin (0Δ, 0Δ, 0Δ). Both the *x* and *y* directions in the simulation and GSM coordinate sets are opposite each other. (b) Time history of the variation of the applied ambient IMF, where the unit along the *x* axis is the time step. Only northward interplanetary field (IMF) is considered.

2. 3-D Global PIC Simulation Model

In the present simulation, we use the same initial conditions to form the magnetosphere, the same radiating boundary conditions and the charge-conserving formulas as those used in our previous works [*Cai et al.*, 2001, 2006a, 2006b, 2009; *Cai and Buneman*, 1992].

2.1. Description of the Model

Within the context of the 3-D global interaction between the solar wind and the magnetosphere, we will focus our attention only on the cusp region dynamics where particle entries through the null points are expected above the cusp region. We expect the kinetic effects to play an important role. Due to computational constraints, the spatial grid is not fine enough to include most of self-consistent instabilities. However, the interaction between the macroscopic electric and magnetic fields and the electrons/ions and their related accelerations are included self-consistently. In this sense, our PIC simulation model is similar to early particle simulation works of beam-plasma interactions, for example, *Buneman et al.* [1966] and *Cai and Buneman* [1992], though at a much higher spatial resolution.

The number of particles within the simulation Debye sphere is about 30, and some particle collisional effects may be expected [*Birdsall and Langdon*, 2004]. Thus, a smoothing technique is applied to reduce the expected noise [*Buneman*, 1993; *Buneman et al.*, 1980, 1992]. An ionosphere model is not implemented, and particles entering the region corresponding to the ionosphere at a distance less than 10Δ (i.e., at distance lower than 2 R_E) are automatically removed from the simulation, where Δ is the grid size. Due to computational constraints, the simulation box in *x*, *y*, and *z* is limited so that the 3-D nearby tail region is included (section 3), but the far magnetotail region ($X > 38\ R_E$) is excluded from our analysis, even if partially included in our simulations. The Alfvén Mach number of the solar wind is relatively low, at about 2.6.

2.2. Simulation Parameters

The simulation domain used in the present three-dimensional PIC simulation is shown in Figure 1a, where $\Delta = 0.2$ *RE* and $\Delta t = 1$ is the time step ($\omega_{pe}\Delta t = 0.125$). Here the grid size is $\Delta = \Delta x = \Delta y = \Delta z$. Initially, we use about 2.2×10^8 electron-ion pairs, which correspond to a uniform particle density of $n_e = n_i = 8$ pairs per cell throughout the simulation box. The time sequence of the IMF application is illustrated in Figure 1b. At time $t = 0$, the center of the current loop that generates the dipole (representing the dipolar terrestrial magnetic field) is inserted in the simulation box at location (160Δ, 137Δ, and 137Δ), and a bulk velocity $V_{solar} = -0.2c$ representing the solar wind is continuously applied within the time range $0 < t < 3000$ along the *x* axis without any IMF. Please note that the speed of light is artificially low, although it is large enough not to interact with other physical phenomena numerically. The injected solar wind density has also $n = 8$ electron-ion pair per cell, and the mass ratio is Mi/me = 16. A northward IMF is progressively applied over the time range $3000 < t < 3150$ and remains constant after $t = 3150$ until the end of the simulation ($t = 9000$), which is

Table 1. List of Normalizations and of Upstream Plasma Parameter Values

Parameters	Normalization	Electron	Ion
Thermal velocity	$\tilde{v}_{\mathrm{the},i} = \frac{v_{\mathrm{the},i}}{\Delta/\Delta t}$	0.125	0.0625
Debye length	$\tilde{\lambda}_{De,i} = \tilde{v}_{\mathrm{the},i}\tilde{\omega}_{Pe,i}{}^{-1}$	1.4	2.8
Larmor gyroradius	$\tilde{\rho}_{ce,i} = \frac{\tilde{v}_{\mathrm{the},i}}{\tilde{\omega}_{pe,i}}$	1.56	12.6
Gyrofrequency	$\tilde{\omega}_{ce} = \tilde{B}, \tilde{\omega}_{ci} = \tilde{B}.r_{\mathrm{mass}}$	0.08	0.005
Inertia length	$\tilde{\lambda}_{ce,i} = \frac{\tilde{c}}{\tilde{\omega}_{Pe,i}}$	4	16
Plasma frequency	$\tilde{\omega}_{Pe,i} = \frac{\omega_{Pe,i}}{\Delta t^{-1}} = \sqrt{\frac{\tilde{q}_{e,i}^2 \tilde{n}_{e,i}}{\varepsilon_0 m_{e,i}}}\,\Delta t$	0.125	0.031
Gyroperiod	$\tilde{\tau}_{ce,i} = \frac{2\pi}{\tilde{\omega}_{ce,i}}$	78.5	1256
Temperature	$\tilde{T}_e = 2\,\tilde{v}_{th,e}^2, \tilde{T}_i = \frac{2}{r_{\mathrm{mass}}}\tilde{v}_{th,i}^2$	0.008	0.032

Parameters	Values
Grid size	$\Delta \cong 0.2$ $RE(=\Delta X = \Delta Y = \Delta Z)$
Time step	$\Delta t \cong 1(\omega_{pe}\Delta t = 0.125)$
Interplanetary magnetic field (IMF)	$B_{IMF} = 0.08$
Particle density	$n_e = n_i = 8$
Speed of light	$\tilde{c} = 0.5$
Solar wind velocity	$v_{sol} = 0.2$
Alfvén Mach number	$V_A = 2.6$
Plasma beta	$\beta = 12$

defined to be when the solar wind particles carrying the IMF has had time to cross the simulation box several times (3.2 times for the present simulations.) The normalized solar wind physical quantities for electrons and ions are defined as follows: thermal velocity: $\widetilde{v}_{\mathrm{the},i} = v_{\mathrm{the},i}/(\Delta/\Delta t)$; Debye length: $\widetilde{\lambda}_{\mathrm{De},i} = \widetilde{v}_{\mathrm{the},i}/\widetilde{\omega}_{pe,i}$; Larmor gyroradius: $\widetilde{\rho}_{ce,i} = \widetilde{v}_{\mathrm{the},i}/\widetilde{\omega}_{ce,i}$; inertia length: $\widetilde{\lambda}_{ce,i} = \widetilde{c}/\widetilde{\omega}_{pe,i}$; gyrofrequency: $\widetilde{\omega}_{ce,i} = \omega_{ce,i}\Delta t = \widetilde{B}\Delta m_e/\Delta t m_{e,i}$; and plasma beta: $\widetilde{\beta}_{e,i} = \widetilde{T}_{e,i}\widetilde{\omega}_{pe,i}/\widetilde{B}$. All normalizations and solar wind parameter values are summarized in Table 1. Hereinafter, we will omit the notation ~ for convenience.

All normalized parameters can appropriately be converted to physical values based on typical real solar wind and magnetospheric plasma conditions. The minimum distance from the Earth center to the dayside magnetopause R_{mp} is about 50 grid sizes. All the physical values are scaled by R_{mp} and the solar wind velocity V_{sw}. If one assumes $R_{\mathrm{mp}} = 64{,}000$ km (i.e., 10 R_E where $R_E = 6400$ is the Earth radius), the solar wind velocity $V_{\mathrm{sw}} = 300$–600 km/s; here 400 km/s is chosen as a typical value, one grid size Δ is about 1280 km, and 1000 simulation time steps represent ~7–14 min or about ~0.64 s per simulation time step. The electron Debye length equals ~1792 km, and the electron thermal velocity equals ~250 km/s. This normalization indicates that only the kinetic effects of space charge and particle acceleration are included. For example, the upstream ion gyroradius is relatively large ($\rho_{\mathrm{ci}} = 12.5\Delta = 2.5\,R_E$ from the top of Table 1) as compared to the physical situation ($\rho_{\mathrm{ci}}(H^+ = 500$–$2000$ km $= 0.078$–$0.31\,R_E$). The gyroradius used here is obtained from a spatial average within the cusp, particularly in the so-called "stagnant exterior cusp." Please see Figure 6 and corresponding text.

3. 3-D Global PIC Simulations: Main Features of the Magnetosphere

3.1. Main Advantages of the Present Simulation

The main advantages (and limitations) of the present simulations are summarized as follows: (i) full self-consistency; (ii) "partial" inclusion of the involved kinetic effects; (iii) simulations are 3-D in physical and velocity space; and (iv) the simulations are global in nature. The included kinetic effects focus on the particle momenta (density and currents) where particles have interacted with macroscopic E and B fields and where both electron/ion momenta quantities can be analyzed and estimated separately (not possible with MHD approach). Most short wavelength instabilities are excluded, and the spatial width of very thin boundary layers are not resolved appropriately, since the simulation grid size is too coarse at present time. While increased

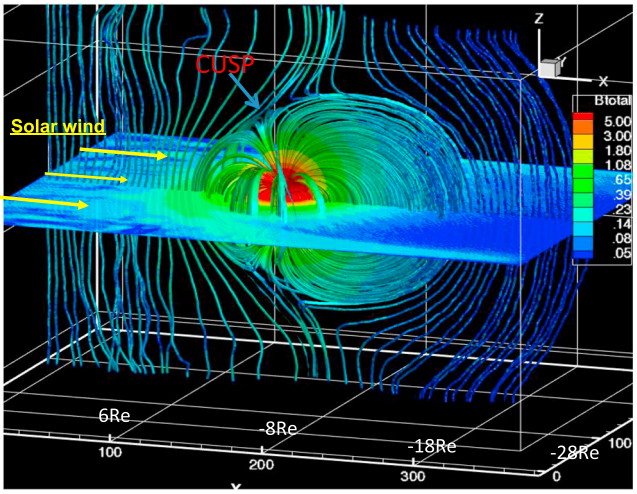

Figure 2. Three-dimensional magnetic field line configuration of the terrestrial magnetosphere under northward IMF conditions at time t=9000. Double scalings in terms of numerical simulation (grid points from the origin (0,0,0) of the box) and GSM coordinate set (origin at the Earth's location) are used along each axis for clarity.

computational performance may be expected to reduce current limitations in the simulations, the basic features of the simulated solar wind-terrestrial magnetosphere interaction are fully implemented in the simulations.

3.2. Main Global Features of 3-D PIC Simulations

In this subsection, we will discuss features of the present global simulations. A discussion of the cusp region is reserved for section 4. Figure 2 shows the global magnetic field configuration for northward IMF orientation. Due to lobe reconnection above the cusp, the magnetic field begins to transit from the dipolar configuration to the tail magnetic field at $x = -24\,R_E$. Figures 4a, 7a, and 8a show possible magnetic reconnection sites at higher latitude above the cusp exterior and magnetopause around the point $(x, z) = (160, 205)$. The pileup of magnetic field on the dayside of magnetosphere and plasma depletions (not shown here) along the draped magnetic field are well represented. Corresponding 3-D global views of ion and electron flux streamlines are shown in Figures 3a and 3b. The electron flux is much noisier than ion flux due to the relatively low number of particles per grid. The electron flux is flapping and weak, although it supports a ring current like flow as illustrated by a circular streamline, indicated by the magenta arrow Figure 3d. Present 3-D PIC simulation (Figure 3c) shows a noticeable oblique flow within the equatorial plane (indicated by the magenta arrow) that is the cross-tail current in the night-dawn side, in good agreement with previous global 3-D MHD simulations [*Ogino et al.*, 1992]

The Rankine-Hugoniot conditions have been verified in the shock region along the subsolar line upstream of the dayside magnetosphere, where the error is within 5%. Altered plasma flow can clearly be seen in Figure 3c. The full spatial features of the shock front, in particular its thickness, cannot be retrieved due to the coarse grid size used in the present simulations (subsection 3.3). However, the details of the shock features are not relevant to the present paper.

3.3. Comparison of the Main Features of 3-D PIC and 3-D MHD Global Simulations

Our simulation results are compared here to those of 3-D global MHD simulation performed by *Wang et al.* [2004] who used UCLA/NOAA global MHD geospace. This simulation model solves the resistive MHD equations with isotropic pressure in a large three-dimensional volume surrounding the Earth, such that the entire interaction region between the solar wind and the magnetosphere, as well as the ionosphere, are included [*Raeder*, 1999].

3.3.1. Shock, Magnetosheath, Magnetopause, and Magnetosphere Layers

Figure 4 compares the total magnetic field magnitude (B_t) in the meridian plane (at $y = 137$) for (a) PIC and (c) MHD simulations. The corresponding ion density N_i for (b) PIC and the plasma density N for (d) MHD simulations are also shown in the figure. The results from the two approaches are similar overall, although the shock layer, magnetosheath, and magnetopause of PIC model are approximately 2 to 2.5 times wider than those of MHD due to the limited scale size of magnetosphere ($R_{mp} = 50\Delta$) used in our PIC simulations. Note that the scale ranges are different for PIC and MHD simulations. The grid size for both PIC and MHD simulation is $0.2\,R_E$, although one grid size in PIC is almost one Debye length. We choose a grid size equal to 1.4 Debye length to avoid numerical instabilities or spurious particles heating [*Birdsall and Langdon*, 2004].

3.3.2. Ion and Plasma Density, and Magnetic Field Profiles Along the Subsolar Line (Line 1)

Different layers between the solar wind and the terrestrial magnetosphere can be identified in terms of B_t (total magnetic field) and N (plasma density) or N_i (ion density) profiles, which are plotted in Figure 5 along the thick, black lines numbered 1 through 5 in Figure 4c and 4d. Herein we will restrict the discussion to these

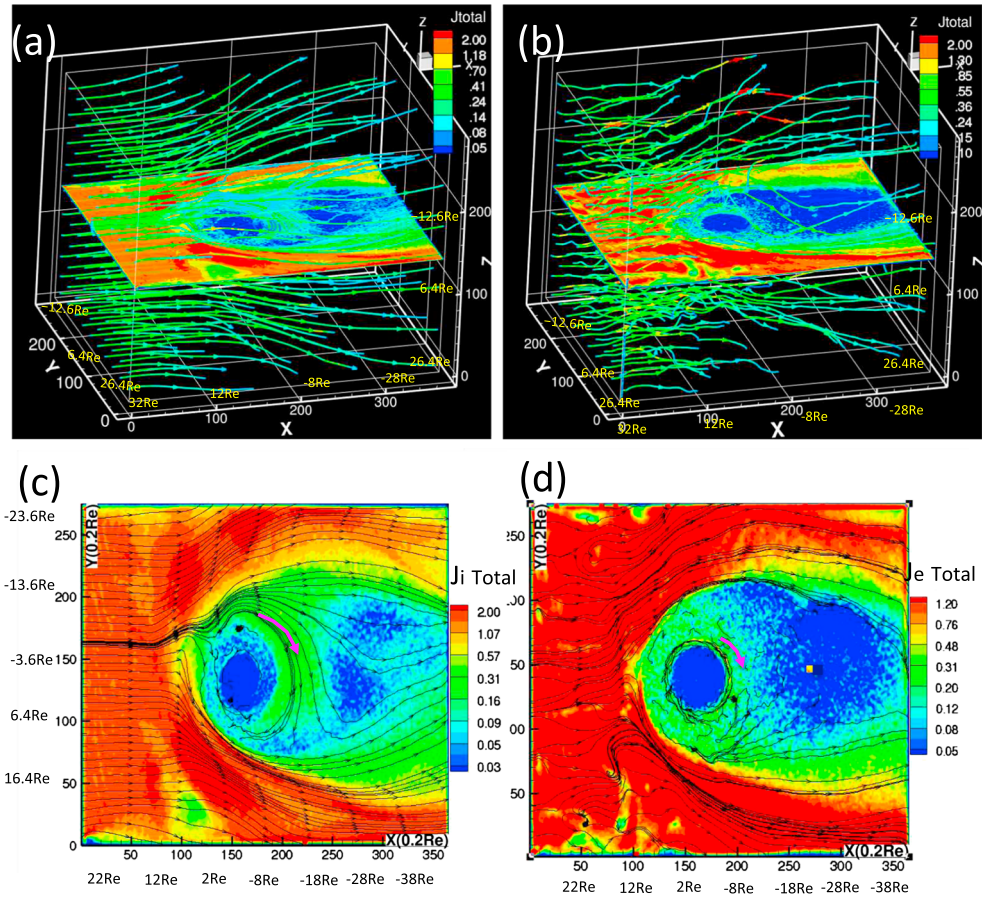

Figure 3. Three-dimensional plot of (a) ion and (b) electron flux streamlines under northward IMF conditions at time $t = 9000$. Corresponding 2-D plots are represented in the equatorial plane (x-y) for (c) ions and (d) electrons. The magenta arrows in Figures 3c and 3d) indicate the direction of the flow.

radial, meridianal cuts for both the MHD and PIC results. Magnetic field strength and ion density sampled along Line 1 are shown as solid lines in Figure 5. The paired blue arrows indicate the shock in Figures 5b and 5e. (whose thickness is indicated between the two blue arrows), in which the right blue arrow indicates the magnetopause boundary in these panels. Sampling along line Line 5 at high latitude is shown as a dash-dotted line. The magnetosheath and magnetopause can be identified in both traces, although the shock is not apparent along Line 5. Figure 5 compares (a) PIC ion density N_i with (d) MHD plasma density N and the total magnetic field magnitude (B_t) resulting from the (Figure 5b) PIC and (Figure 5e) MHD simulations. The variation of Log M_A (where M_A is the local Alfvén Mach number) is displayed in Figure 5c for the PIC simulation only.

In Figure 5, the shock layer is characterized by the increase of both N (or N_i) and B_t, as compared with upstream values. Moreover, in the northward IMF configuration with relatively low Alfvén Mach number ($M_A = 2.6$) as in our case, it is often found that the magnetosheath has a so-called slow mode structure [*Zwan and Wolf*, 1976], where the spatial variation of the density ΔN is opposite to that of the magnetic field ΔB. More precisely, inside the magnetosheath (located between the shock front and the MP), we can identify two different regions A and B (shown in Figures 5b and 5e) for Line 1, where the spatial variation ΔB is negative and, thus, ΔN is positive (first half upstream magnetosheath or region A) and where the variation ΔB is positive and ΔN is negative (second half upstream magnetosheath or region B.) Region B shows one of the slow mode signatures where the variation ΔB is positive and ΔN is negative, which is sometimes referred to as the plasma depletion layer (PDL) [*Zwan and Wolf*, 1976]. The magnetopause (MP) can be characterized by the last closed Earth magnetic field line with a smaller decrease in the slope of N and a smaller increase in the slope of B_t as compared with the upstream values.

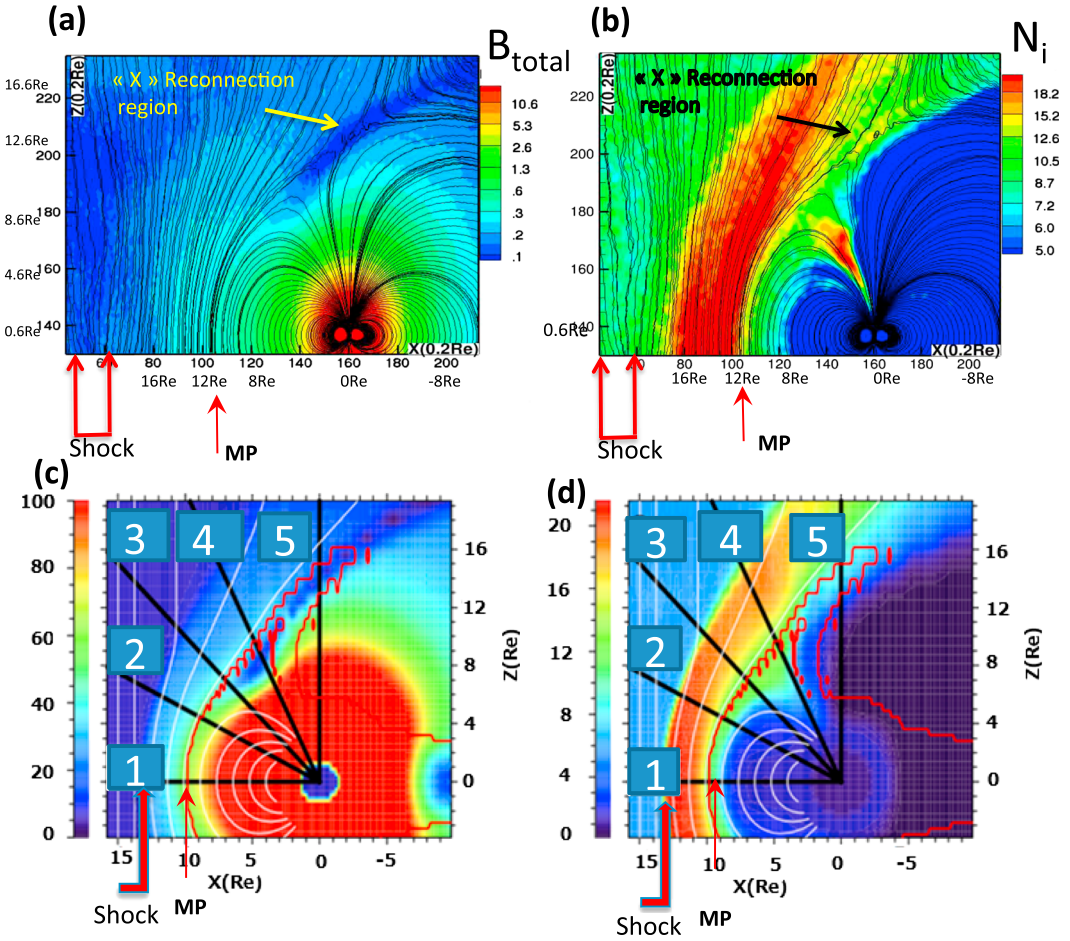

Figure 4. Comparison of results obtained with the (a and b) present 3-D PIC simulation and (c and d) with 3-D MHD simulation by *Wang et al.* [2004] for (Figures 4a and 4c) total *B* field and (Figures 4b and 4d) ion density, respectively, under purely northward IMF. The results correspond to simulation data obtained on the North Hemisphere cusp region indicated by the arrow in Figure 2. The thick and thin red arrows indicate the locations of the bow shock and of the magnetopause (MP), respectively, along the *X* axis. The numbers 1–5 define the radial slicing lines used in Wang et al. Figures 4c and 4d and Lines 1 and 5 are reported in Figure 5. Plots are from the meridian plane.

The density profiles shown in Figures 5a and 5d along Line 1 going from upstream to downstream show increases of about 20% and 175% for the PIC and MHD, respectively. In region A (or the upstream magnetosheath) the PIC ion density N_i and MHD density N increase by about 100% and 1–2%, respectively, as compared with the upstream density values. In region B (or the downstream magnetosheath) the PIC ion density N_i and MHD density N decrease by about 40% and 50%, respectively. Along Line 1, *Wang et al.* [2004] have shown that flux tubes become draped around the nose of the magnetosphere, resulting in magnetic field pile-up accompanied by a corresponding depletion of plasma that maintains constant plasma pressure.

Let us more carefully compare the results shown along Line 1 in Figures 5a and 5b between $15.5\,R_E > x > 12.5\,R_E$. In Figure 5b, there is a bump (ΔB) in B_t superimposed on a continuous increase (between $16\,R_E > x > 8\,R_E$), while the density N_i exhibits a depletion (negative ΔN) which is characteristic of a slow wave structure. This signature is not evident in the MHD results in the same region; however, a localized bump in *B* and anticorrelated depletion in *N* is found between $11.7\,R_E > x > 8\,R_E$. These differences in the MHD and PIC results are likely due to the different scales and deformation of the overall magnetosphere caused by differing upstream plasma conditions (unfortunately the Mach regime is not indicated in *Wang et al.* [2004]).

3.3.3. Ion and Plasma Density, and Magnetic Field Profiles Along the Polar Line 5

The polar B_t and N_i profiles along Line 5 are quite different from the subsolar values along Line 1 as shown in pairs in Figures 5a and 5d and Figures 5b and 5e from the PIC and MHD simulations, respectively. Along Line 5,

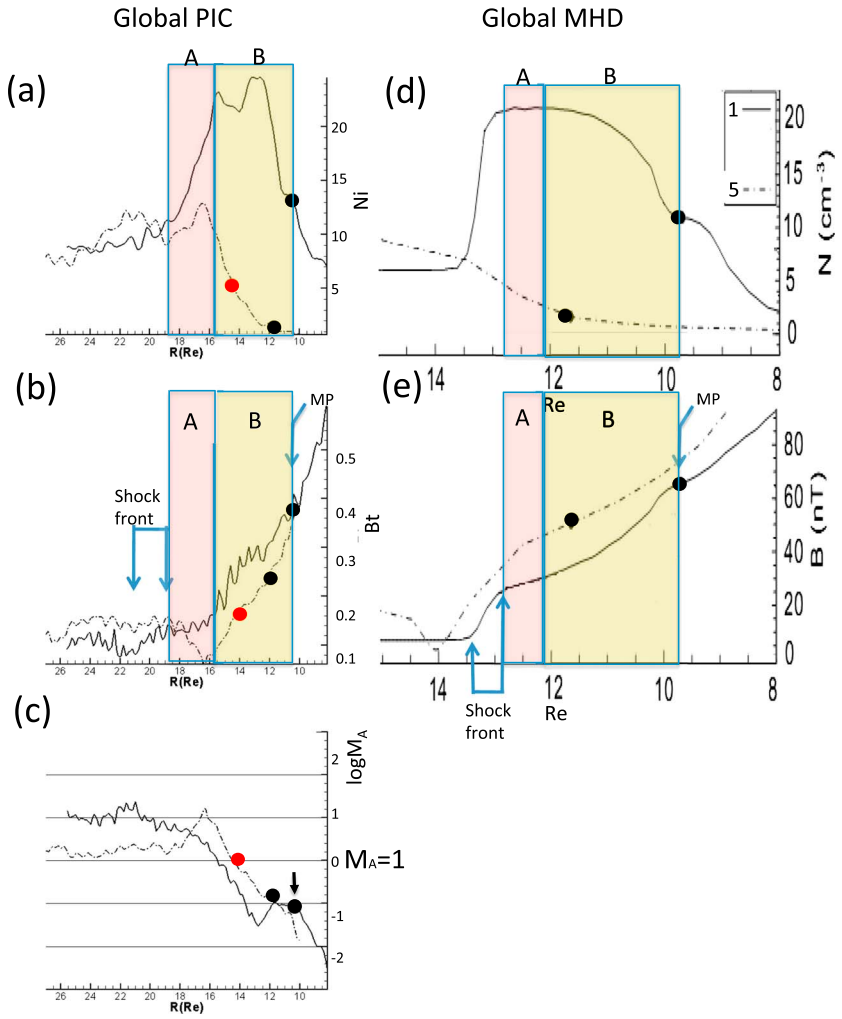

Figure 5. Comparison is shown between 3-D PIC and 3-D MHD simulation results measured along the slicing Lines 1 (solid line) and 5 (dashed line) defined in Figures 4c and 4d; (a) Ion density N_i, (b) total magnetic field B_t, and (c) logarithm of M_A (where M_A is the local Alfvén Mach number) that is valid for the PIC simulation, while Figure 5d is the plasma density N and Figure 5e total magnetic field B_t valid for MHD simulation. The red circle indicates the transition from a super to sub-Alfvén flow regime (Log(M_A) = 0). The red circle is defined along Line 5 (which crosses the cusp region, see Figures 4c and 4d) in Figures 5a–5c. The black circles in Figures 5a–5e define the location of the last closed terrestrial magnetic field line, i.e., the location of the magnetopause (MP, indicated by one blue arrow). The bow shock location is defined with vertical arrows in Figures 5b and 5c and obtained from Figure 4. The distance between arrows provides the shock thickness. The area between the shock and the magnetopause defines the magnetosheath, which is composed of two areas A and B (see text). The spatial scale used along Lines 1 and 5 is the same and corresponds to that along the X and Y axis in Figures 4c and 4d, respectively. The black arrow in Figure 5c indicates that this is from Line 1.

no shock layer can be clearly identified. However, opposite signatures in ΔB and ΔN are found in the PIC simulation across a possible magnetic X reconnection site, where the magnetic field and density show narrow V-shaped and inverse V-shaped decreases and increases, respectively. These anticorrelated profiles are characteristic of crossing a weak magnetic field region related to the possible high-latitude reconnection site indicated in Figure 4a.

Similar aniticorrelated B and N profiles, indicative of reconnection, are also observed in satellite observations. For example, similar N and B_t profiles were observed during an Interball satellite crossing from the high-latitude magnetopause (downstream) to the magnetosheath (upstream) under stable northward IMF [*Avanov et al.,* 2001]. From the magnetosheath to the magnetopause, the density N decreases by factors of about 8–9 and 7–8 for the PIC simulation and the Interball observation, respectively. Correspondingly, the magnetic field amplitude B_t increases about 70% and 40% for the PIC simulation and the Interball observations, respectively.

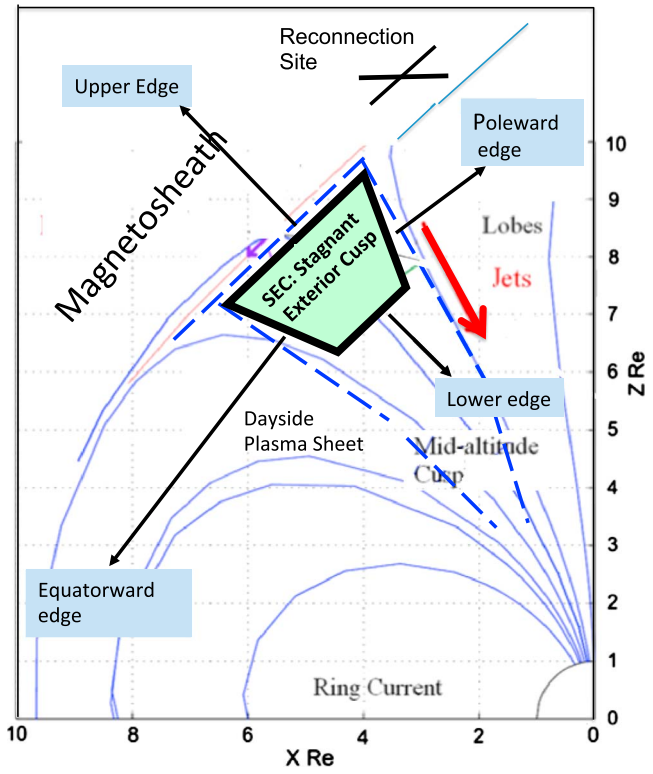

Figure 6. Schematic sketch of the cusp region, its surrounding boundaries, and main areas (adapted from *Lavraud et al.* [2004]). The trapezoid indicates the location of the stagnant exterior cusp (SEC), where the perpendicular convection flow (V_{perpX}) is very weak.

This decrease in density and increase in magnetic field causes the magnetospheric directed flow to transition from super to sub-Alfvénic such that the reconnection site stays almost stable and stationary in this high-altitude region [*Avanov et al.,* 2001; *Fuselier et al.,* 2000a, 2000b]. On the other hand, the anticorrelated V-shaped *B* and inverse-V-shaped *N* "slow mode" structures shown in Figures 5d and 5e are not evident in the MHD simulations of *Wang et al.* [2004]. This difference may be due to different simulation parameters and the associated deformations of the Earth magnetosphere. In the PIC simulation the flow transitions from super to sub-Alfvénic (Figure 5c and subsubsection 4.2.4) in the area where B_t and *N* increases and decreases, respectively.

4. Main 3-D Global PIC Simulation Results on the Magnetic Cusp

In this section, we discuss the ability of our PIC simulation to retrieve basic features of the magnetic cusp. Three-year statistical survey of Cluster cusp data by *Lavraud et al.* [2005] provides the opportunity to compare simulation results using a similar local mapping of the cusp region in the meridian plane to identify where it works and where it does not. The previous experimental work by *Lavraud et al.* [2004] provides a schematic view of the cusp (Figure 6) that will be used here as a reference. In Figure 6 the adjacent closed field line region equatorward of the cusp is called the dayside plasma sheet [*Borovsky et al.,* 1998].

4.1. Main Features of the Magnetic Cusp From 3-D PIC Simulations

4.1.1. Magnetic Fields

The magnetospheric cusp is commonly identified as a high-latitude region populated by particles with shocked solar wind energies and densities near local noon, along with turbulent or depressed local magnetic fields [*Dunlop et al.,* 2000; *Pu et al.,* 2004; *Zong et al.,* 2004]. First, we compare magnetic field lines resulting from our PIC simulation, shown in Figure 7a, with a vector plot of the statistical magnetic field derived from the Cluster survey by *Lavraud et al.* [2005], as shown in Figure 7b. This is where the pile-up of *B* field lines is observed at the outer edge of the cusp, adjacent to the nightside lobe.

Figure 7a shows the northern magnetospheric tail lobe and the pileup of *B* field lines at the outer edge between the cusp and the nightside lobe. A possible reconnection site is above and tailward from the cusp, and the related weak *B* field area spreads along the magnetopause (toward nightside). This implies an open magnetosphere and possible high-latitude reconnection for a northward IMF orientation. More drapped magnetic field lines are observed at higher latitude near the reconnection region (not shown). In Figure 7b, the distribution of the magnetic field vector corresponds to a projection using the transformation described in *Lavraud et al.* [2004, 2005] and the size of each vector represents the logarithm of the magnitude of the magnetic field, $|B|$. The color of the vectors corresponds to the absolute value of deviation of the measured *B* field from the T96 model, where T96 model is the Tsyganenko magnetic field model [*Tsyganenko,* 1996]. In order to compare our PIC simulation results with $\delta|B - BT96|$ from Cluster observations shown in Figure 7b, similar analysis has been performed using PIC results and are shown in Figure 7c. The trapezoid

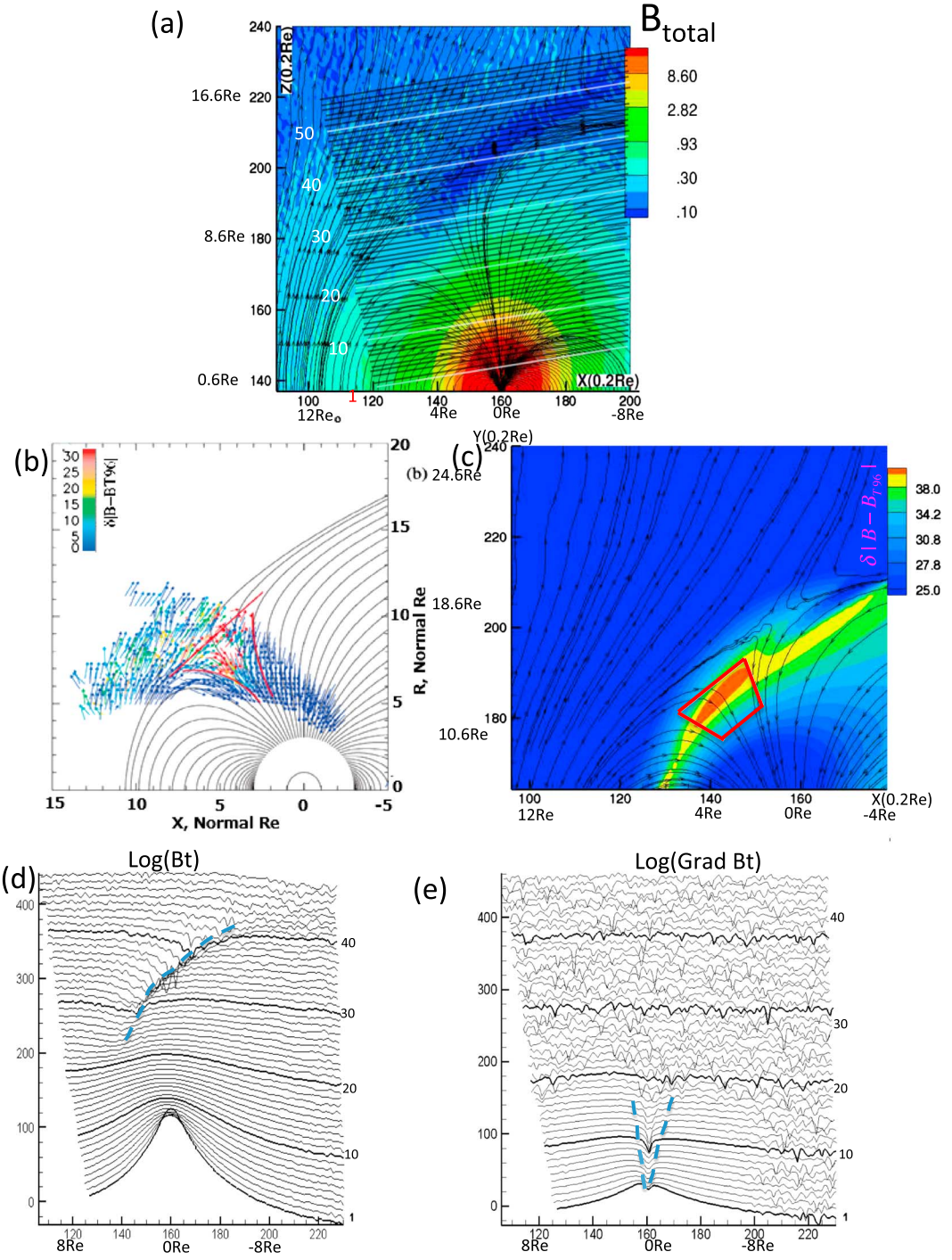

Figure 7. (a) Magnetic field results found from PIC simulations with locations of the corresponding perpendicular slicings in the meridian plane. The identification number of the slicings increases from 1 to 48 with distance from the Earth. (b) Cluster observations in the meridian plane (*X-Z*) where the vector colors are δ|B-BT96| and where BT96 is the *B* field obtained from the Tsyganenko magnetic field model (from *Lavraud et al.* [2005]). The size of each vector is the logarithmic amplitude of the *B* field. Similarly, a contour plot of δ|B-BT96| are applied to PIC simulation results with similar contour color and are shown in Figure 7c. Stackplot of the amplitude of the (Figure 7c) total *B* field and of (Figure 7d) Gradient B versus distance, as measured along the perpendicular slicings defined in Figure 7a. In the Figures 7d and 7e stackplots, the *x* axis corresponds to the *x* axis in Figure 7a, and the *y* axis units are arbitrary.

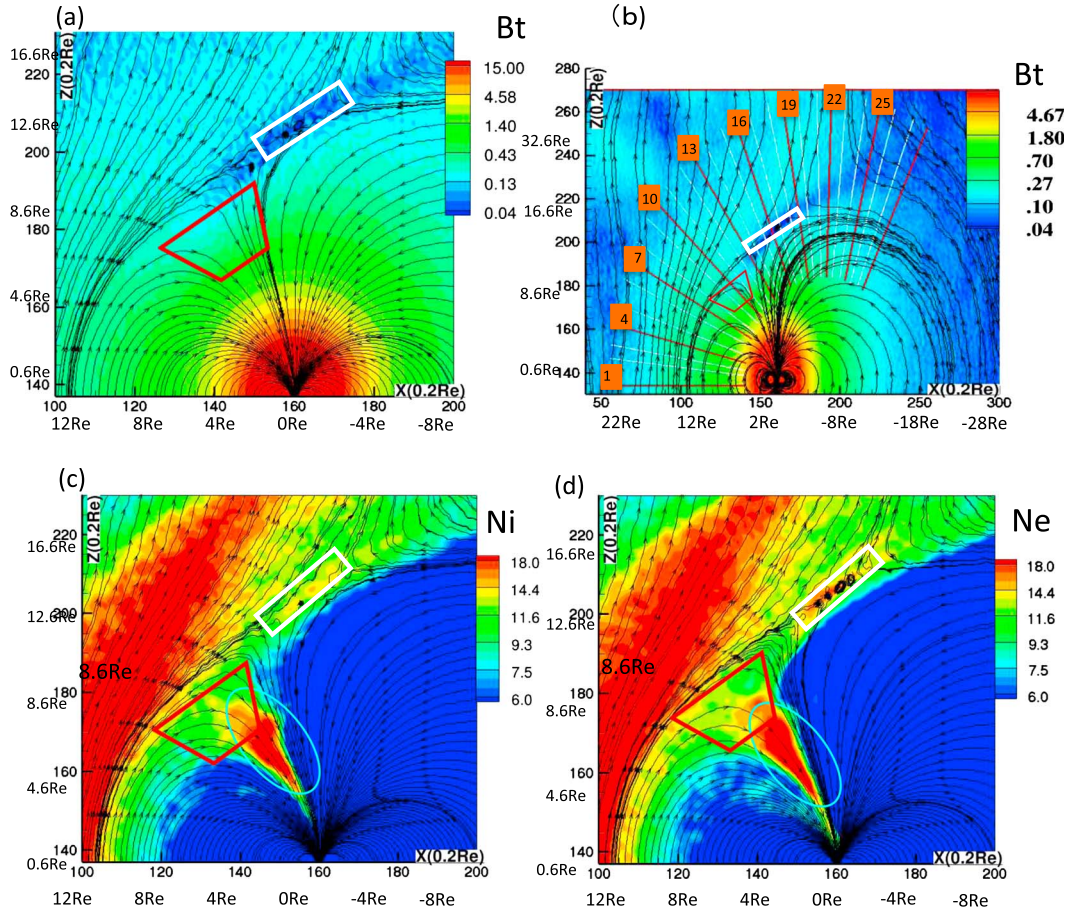

Figure 8. (a) Color is used to represent the magnitude of B_t and field lines also plotted in the meridian plane *X-Z*; and (b) a plot similar to Figure 8a with extended axes and numbered radial slicings are provided as reference for use in Figures 9b and 9c. The corresponding colored coded mapping of density is shown for ions and electrons in Figures 8c and 8d, respectively, where the *B* field lines are superimposed for reference. The red trapezoid indicates the location of the stagnant exterior cusp (SEC). The white rectangles (in Figures 8a, 8c, and 8d) indicate a possible X reconnection region where *B* is very weak.

in Figure 7c indicates the stagnant exterior cusp (SEC) region—or SEC—as defined in Figure 6. Results show that trapezoid location in PIC results is slightly (about 5°~10°) shifted toward lower latitude with respect to the Cluster results. The difference is discussed in section 5. Despite this difference, reasonable agreement is obtained between our PIC and the Cluster results: (i) the absolute value of the *B* field difference (red part) is strongest in the upper part of the section in both of the cases shown (Figures 7b and 7c), and (ii) the direction of *B* vectors (Figure 7b) and of model *B* field lines (Figure 7c) show a well-draped magnetic field topology close to the outer boundary as expected for a northward IMF configuration.

However, an open magnetosphere with possible high-latitude reconnection for northward IMF requires more precise criteria in order to clearly identify the magnetic cusp. Figure 7d shows a stackplot of $|B|$ profiles sampled perpendicular to the cusp center line in the meridian plane as illustrated in Figure 7a (and are referred as "perpendicular slicings" in what follows). The perpendicular slicing numbers of Figure 7a are reported in Figures 7d and 7e. The *x* axis in Figures 7d and 7e stack plots correspond to the *x* axis in Figure 7a. The *y* axis units are arbitrary. For low-altitude perpendicular slicings in Figure 7d, the cusp boundary is too wide to use the inflection points of the total magnetic field profile in order to define the magnetic cusp region. As altitude (line number) increases, the left-hand side weak magnetic field region in the dayside (Line = 21~28) connects to the weak magnetic field region that corresponds to the possible high latitude reconnection site (Line = 29~42). The reconnection related weak magnetic fields extend downward in altitude from Line = 42 to Line = 29. The width of the characteristic V-shaped weak *B* field profile is about 2–4 R_E in the possible reconnection area (where the center is indicated by a thick dashed blue curve in

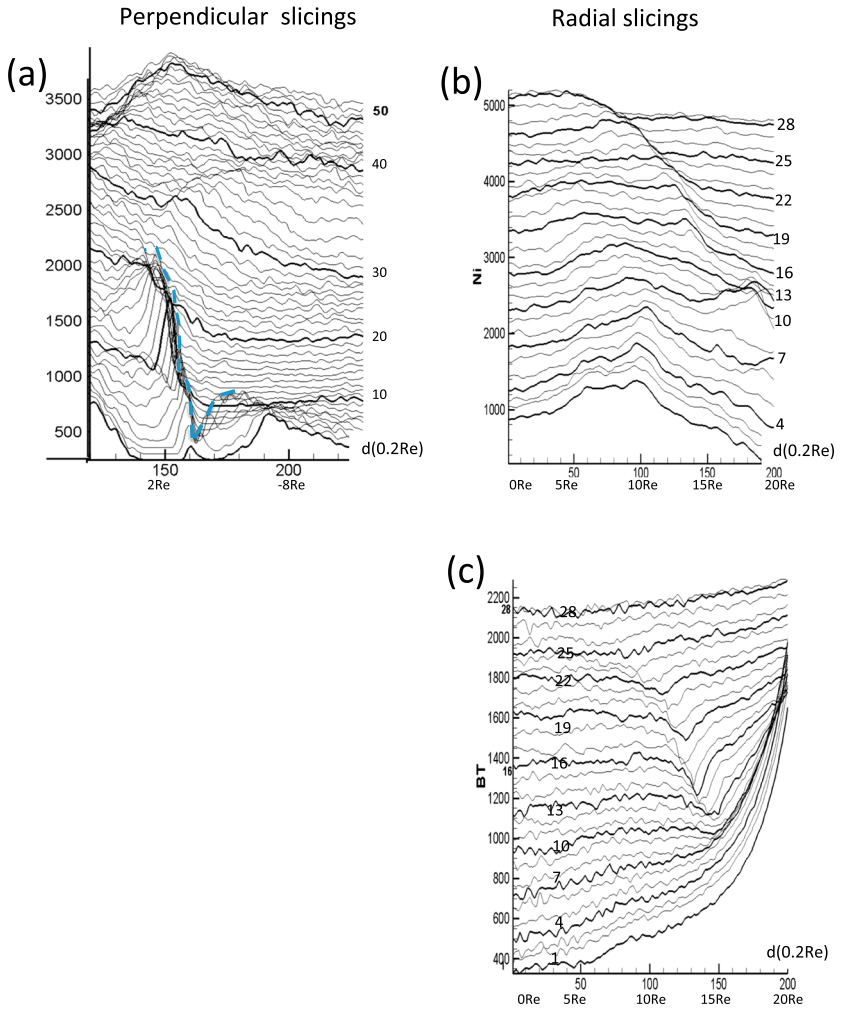

Figure 9. Stackplots are shown of perpendicular and radial slicings of the (a and c) ion density N_i and the (b) total magnetic field B_t, respectively. These slicings are defined in Figures 7a and 8b, respectively. For perpendicular slicings, the scale along the horizontal axis (Figure 9a) corresponds to the scale of the slicing projected onto the x axis. For radial cuts, the x axis is the distance d that is measured such that increasing value is inward from the starting point (upward) to the end points (downward). Along Line = 1, the values $d = 0$ and 200 correspond to $x = 55$ and 140, respectively. For all panels the y axis units are arbitrary.

Figure 7d); the depth of this profile decreases when moving toward lower altitude where it connects to the SEC (Figure 6) as shown in Figure 7d.

Second, instead of using B_t, perpendicular slicings of Log(∇B_t) values are calculated and plotted in Figure 7e. The two dashed lines that connect local maxima values in this figure are a simple and good diagnosis to identify the magnetic cusp boundaries at low altitude; however, in the high-altitude region (Line > 19), they become too noisy and are not appropriate any more. The diagnosis of Figures 7d and 7e are complementary. Regardless, a more precise diagnosis is necessary to define the cusp region at high altitude where, in particular, the section is expected.

4.1.2. Ion and Electron Densities

Let us focus now on the ion and electron density contours within the same meridian plane that are shown in Figure 8. The red trapezoid indicated in the plots represents the schematic boundaries of the SEC as is in Figure 6. The white rectangle in each panel indicates the location of a possible high-latitude reconnection site. Figure 8b also indicates the locations of radial slicing lines (Line = 1–28) that are used for the stack plots shown in Figures 9b and 9c. These lines are almost perpendicular to the interior magnetospheric magnetic field although the apex of the converging lines is shifted slightly tailward to (x, z) = (190, 137). Within the

magnetic cusp, a strong density peak is observed for both electrons and ions from the lower edge of the SEC to the lower cusp region and is identified with a light blue ellipse in Figures 8c and 8d. Above the upper edge of the SEC, electron and ion densities have relatively large values, which are correlated to weak total magnetic field amplitudes that extend through the reconnection region (white rectangle). Let us analyze more carefully the B_t and N profiles along the perpendicular and radial slicings as defined in Figures 7a and 8b. Figure 7a sampling is used in Figures 9a, and Figure 8b sampling is used in Figures 9b and 9c.

A well-defined peak in density is observed for the cusp in the stackplot Lines 1–24 in Figure 9a. The peak is marked by a thick dashed blue line. As the altitude increases, this peak density reaches a maximum around Line~10–12 above which is decreases and shifts to the equatorward edge (as defined in Figure 6), merges with the high plasma density region (possibly the equatorward dayside plasma sheet as indicated in Figure 6), and then disppears at Line $>$ 25. Please note that in Figure 9a the range of cuts is greater than that indicated in Figure 7a.

The distances, in simulation grid units d, along the horizontal axis in Figures 9b and 9c start from zero well away from the Earth and end at the convergent vertex of the slicing lines, defined in Figure 8b, just tailward of the Earth. Slicing Line 1 falls along the Sun-Earth line. First, a noticeable increase of the ion density N_i and the total B_t amplitude can be identified in the radial slicing Lines 1 to 10 within the spatial range $0 < d < 120$. These layers correspond to the dayside shock layer and magnetosheath regions that includes the slow modes, from left (upstream) to right (downstream), as already discussed in subsection 3.3.2 for Line = 1 (in Figures 5a and 5b).

Second, with increasing latitude or radial slicing number Line, the variations in B_t and N_i are anticorrelated; i.e., a local decrease of N_i is associated with a local increase of B_t or vice versa from Lines 13 to 20, within a part of the range $110 < d < 170$ that corresponds to the reconnection related region. In this region, B_t presents a V-shaped profile with a deep local minimum in Line~17, and N_i has a corresponding local maximum. These localized variations correspond to the slicing line that passes through the middle of the possible X reconnection region, highlighted by the white rectangles in Figure 8. The high-density plasma in the middle altitude cusp shown in Figures 8a–8d can be seen in slicing Lines ~9 to 14 (for $165 < d < 200$). With these radial slicings, the SEC upper boundary located both around Lines 8 through 12 for $150 < d < 180$ appears between two areas that correspond to the downstream boundaries of the dayside magnetosheath and the high-latitude reconnection region.

4.2. Main Features of the 3-D Global PIC Simulation Compared With Cluster Satellite Observations

4.2.1. Stagnant Exterior Cusp (SEC) Region

As discussed in section 4.1, the magnetic cusp region can be relatively well defined by the spatial profiles of gradient B and density for low to middle altitudes. A typical SEC or diamagnetic cusp region was schematically defined by *Lavraud et al.* [2005], based on statistical observations made by the Cluster satellites. According to *Lavraud et al.* [2004, 2005] for a northward IMF configuration, the SEC region is bounded by distinct poleward, upper, lower, and equatorward edges as shown in Figure 6. The poleward edge is characterized by both downward field aligned (FA) ion jets and its correlated perpendicular flow. The upper edge is characterized by a transition from super-/sub-Alfvénic flow regime (see section 4.2.4). The equatorward edge has no specific features, except it represents the link between the cusp region and the dayside plasma sheet. Let us verify what features can be retrieved (or even improved) in the present 3-D PIC simulations.

4.2.2. Field Aligned (FA) Flows

The statistical results derived from the Cluster mission are shown in Figure 10a. The main features are (1) a large upward field aligned (FA) ion flow in the magnetosheath region (black ellipse), (2) a downward FA flow in the magnetosphere lobe edge (light blue circle), (3) upward FA flows at high latitude around $x = 2$–$4\,R_E$, $y = 6$–$9\,R_E$ (blue rectangle near the poleward edge of the cusp shown in Figures 10c and 10d), which are correlated with sunward convection that will be discussed in the next subsubsection, and (4) the lack of upward FA flow (no red dots) corresponding to an almost stagnant region at the equatorward edge near the plasma sheet boundary. Note that the terms "downward" and "upward" mean $V_{//} < 0$ and $V_{//} > 0$, respectively. These distributions suggest the occurrence of reconnection at the high-latitude lobe magnetopause.

The upward FA beam (red dots) at high latitude inside the SEC seems to be correlated with sunward convection near the poleward edge and tailward convection at lower latitude (see Figure 10c and section 4.2.3).

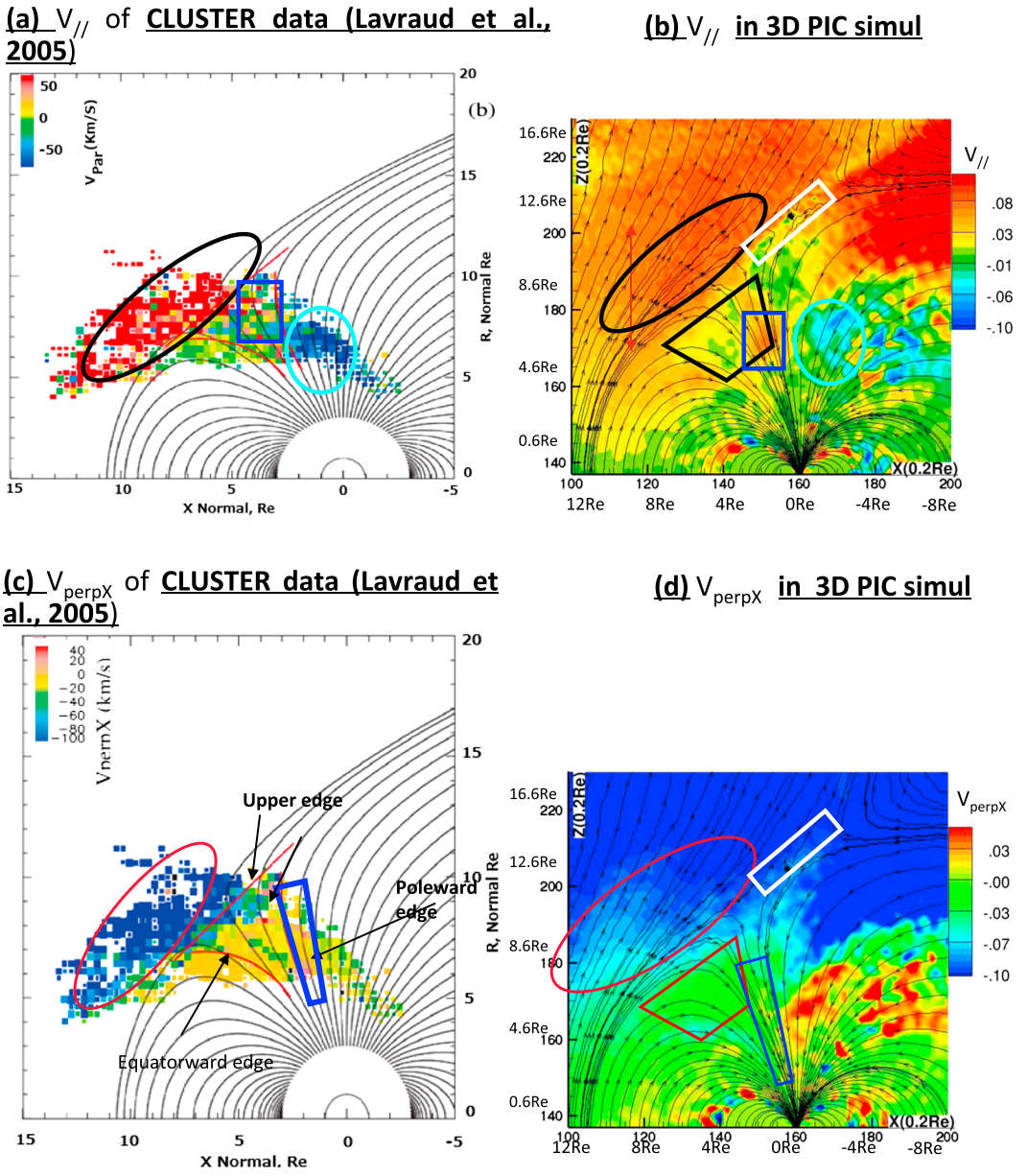

Figure 10. Colored contour plots of FAB (Field Aligned Beam) ion flow in the meridian plane obtained from (a) the Cluster statistical survey is compared with (b) PIC simulation results; and $V_{//} < 0$ (>0) indicates the direction opposite to (same to) the *B* field. Contour plots of V_{perpX} ion flow in meridian plane obtained from (c) the Cluster statistical survey are compared with (d) PIC simulations; and $V_{perpX} < 0$ (>0) indicates the tailward (sunward) direction.

A comparison of PIC simulation results shown in Figure 10b with the Cluster satellite results in Figure 10a, where a similar color spectrum is used has been performed and leads to the following observations:

1. The amplitude of the FA beam in the simulation is about 10% lower than that observed by Cluster in the magnetosheath. However, overall, a reasonable correspondence of regions with $V_{//} > 0$ and $V_{//} < 0$ is found.
2. The relative location of the identified regions (rectangle and light blue circle) are slightly shifted one from each other due to the difference in solar wind Mach regime between the simulation and observational period, which may be expected to influence the shape of the cusp region. In particular, in PIC simulation, the area where $V_{//}$ is almost zero is shifted to higher latitude, and the $V_{//} < 0$ region correlated with tailward convection flow (see Figure 10c and subsubsection 4.2.3) is observed at both higher latitude and higher altitude (light blue circle in Figure 10b).

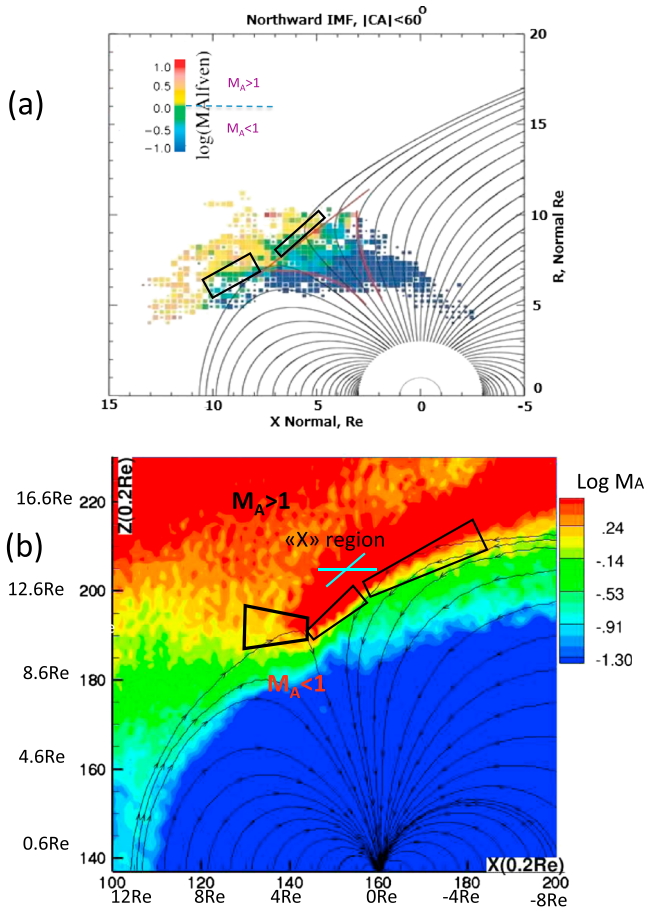

Figure 11. Colored contour plots of the logarithm of M_A where M_A is the local Alfvén Mach number obtained for (a) the Cluster statistical survey and (b) PIC simulation for Northward IMF configuration. Plots are represented within the meridian plane and only the magnetospheric *B* field line is plotted.

More generally, a one-to-one quantitative comparison cannot be performed at the present stage of the investigation. Indeed, present simulation results are based on one unique simulation performed for a given set of upstream parameters (in particular, for a fixed flow of the solar wind and for purely northward IMF configuration). Moreover, all samplings have been made within the meridian plane in order to simplify diagnostics. In addition, the PIC simulation is based on a "best" compromise for the upstream properties as compared with the real values, because of the computational constraints. On the other hand, the Cluster statistical results are based on multiple cusp crossings and a range of solar wind conditions for only approximately northward IMF. In addition, all results have been projected on a 2-D model of the meridian plane that smooths 3-D behavior. It remains for us to examine the quantitative impact of such upstream parameters variations and of the 3-D behavior projection into the meridian plane. These limitations continue in the next section. The full patterns of 3-D behavior of the IMF oblicity and of different Mach regimes are left for further study.

4.2.3. Perpendicular Convection Flow

Perpendicular ion convection V_{perpX} is shown in Figure 10c and 10d using a color scheme similar to that in Figure 10a and 10b, where the magnetosheath, the stagnant exterior cusp (SEC), and poleward edge are mapped. We observe strong tailward convection ($V_{perpX} < 0$) in the magnetosheath (red ellipse) and weak tailward convection in SEC (red trapezoid). In contrast, sunward ($V_{perpX} > 0$) convection is only observed in the PIC simulation in narrow areas at middle and low altitudes (blue trapezoid), which can be mapped to and are consistent with similar areas in the statistical Cluster results (blue trapezoid). For both PIC and Cluster results, the blue and red distributions that correspond to tailward and sunward convection area, respectively, are slightly shifted one to the other because of different upstream conditions as discussed above in section 4.2.2 (Figure 10b). In both cases within the SEC, the tailward convection flows are relatively weak (yellow to yellow-green area), nearly stagnant.

A comparison of FA and perpendicular convection shows that the upward FA flow (red) at high latitude in Figure 10b (blue rectangle) seems to be (partially) correlated with sunward convection near the poleward edge (blue trapezoid in Figure 10d) and tailward convection at lower latitude. These features are in good agreement with observations by *Lavraud et al.* [2005]. The feature suggests that this noticeable flow could be due to particle gyromotion (here we have only a 2-D cut of flow streamlines) that needs further analysis.

4.2.4. Transition Layer From Super-Alfvénic to Sub-Alfvénic Regime Adjacent to SEC

The distribution of the logarithm of the local Alfvén Mach number (M_A) in the high-latitude cusp region obtained from *Lavraud et al.* [2005] is shown in Figure 11a. These results clearly show that for northward

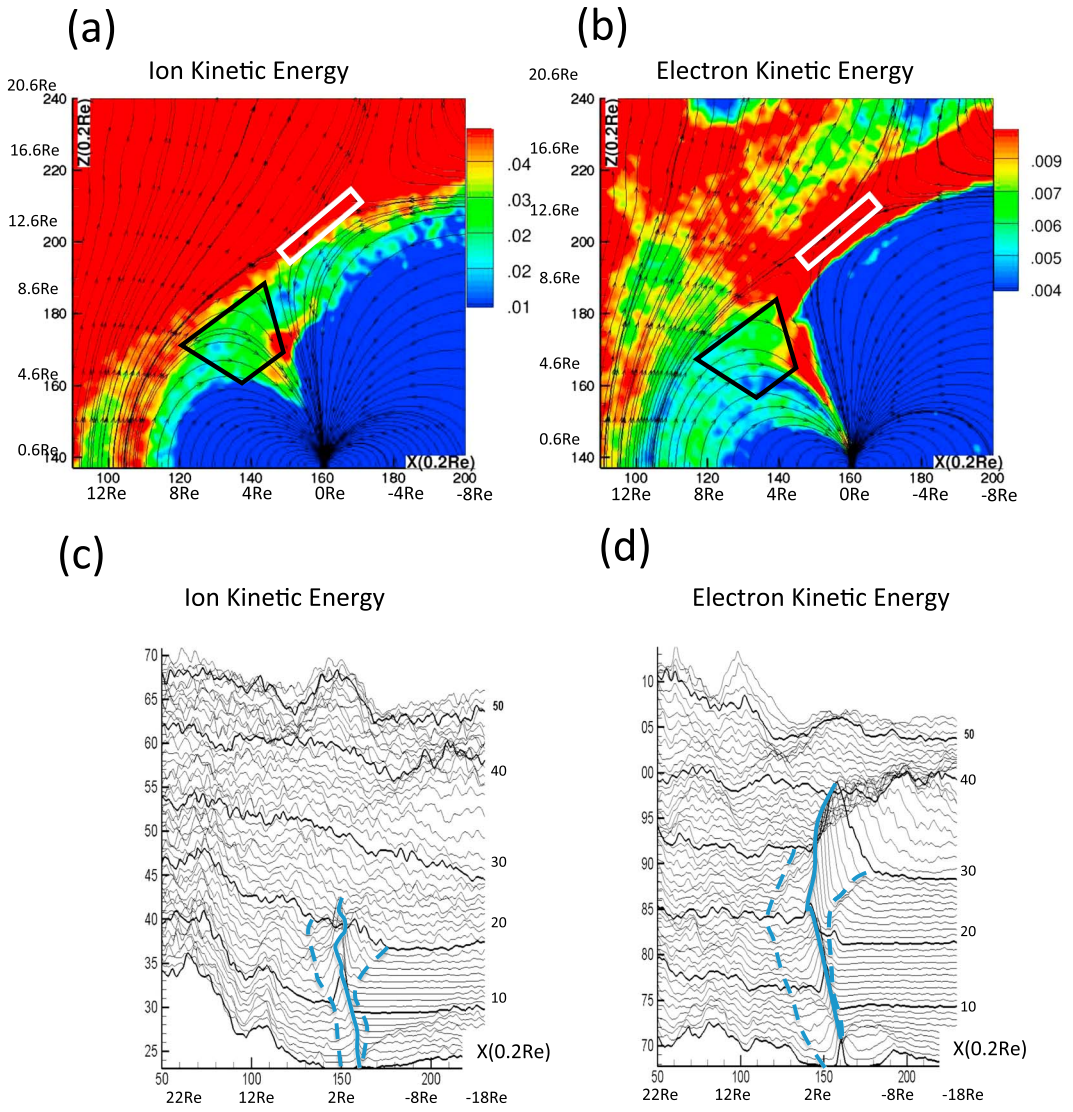

Figure 12. Colored contour plots of kinetic energy density (average $v_x^2 + v_y^2 + v_z^2$ of the particles in each simulation cell) obtained for (a) ions and (b) electrons in the meridian plane. Results are obtained for the 3-D PIC simulation only. Corresponding stackplot of (numbered) perpendicular slicings obtained for (c) ions and (d) electrons; locations and numbering of the slicings are defined in Figure 7a. For perpendicular slicings, the scale along the horizontal axis (Figures 12a and 12b) corresponds to the scale of the slicing projected onto the *x* axis in Figure 7a. The *y* axis units are arbitrary.

IMF, the flow is super-Alfvénic within the magnetosheath, becoming sub-Alfvénic when penetrating the upper edge of the stagnant exterior cusp (SEC) region. Consequently, a boundary layer where M_A ~1 may be defined. For comparison, a similar mapping of local M_A values from our simulation are displayed in Figure 11b. Striking features are that (a) a similar boundary layer is reproduced in the 3-D PIC simulation at the same location, which we will refer to as the Alfvén transition layer (ATL), and (b) the ATL is clearly and continuously extended out of the cusp region in the meridian plane. More precisely, in the PIC simulation (Figure 11b) the ATL seems to be located at larger radial distance, outward from the SEC, than that found in the Cluster results. *Lavraud et al.* [2005] have described this region as the Plasma Depletion Layer (PDL). Simply, the PDL layer corresponds to a simultaneous increase of the magnetic field magnitude B_t and a decrease of the plasma density *N* in conjunction with upward flow. The flow transitions from super-Alfvénic to sub-Alfvénic across the PDL. Retrieving all features of the PDL requires more extensive analysis, which is beyond the scope of the present work. Here we will differentiate ATL from PDL, focusing on the features of the so-called ATL (in terms of transition from super- to sub-Alfvénic flow).

One advantage of the present PIC simulation results with respect to Cluster data is ability to make an extended mapping of the so-called ATL. This layer extends slightly sunward for both PIC and statistical studies. In addition, PIC simulations show that (i) the sunward part of the ATL largely extends much more toward the dayside than indicated in the Cluster study, which did not include this region; (ii) the tailward part of the ATL approaches the possible magnetic reconnection region (illustrated by "X" in Figure 11b) with a width that progressively increases (as illustrated by successive elongated trapezoids); (iii) these two parts of the ATL meet at the middle of the upper edge of the SEC, where the width of the ATL is a minimum (i.e., steepening of the layer is the largest, suggesting a possible acceleration mechanism); and (iv) the X region is slightly above the ATL.

4.2.5. Ion and Electron Kinetic Energy Densities

PIC simulation results for cell-average ion and electron kinetic energy densities $\left(< v_x^2 + v_y^2 + v_z^2 >\right)$ are shown with stackplots of associated perpendicular slicings (same as those defined in Figure 7a) in Figure 12. The ability to obtain particle energies is one of the important advantages of PIC simulations. The SEC region is annotated for reference and a white rectangle indicates a possible X reconnection region. In agreement with satellite observations [*Cargill et al.,* 2005; *Lavraud et al.,* 2002], the cusp is shown to be characterized by high kinetic energy particles, which can be used as tracers to define the cusp region.

The kinetic energy features most relevant to our discussion are (i) strong peaks of both ion and electron energies are clearly identified, which allow us to readily define the low and middle cusp regions as illustrated by full and dashed lines in Figures 12c and 12d; (ii) the peak in ion energy corresponds to strong upward FA ion flow ($V_{//} > 0$) near the lower edge of SEC (Figure 10b); (iii) Figure 8c shows a region of enhanced ion density extending into the deep cusp region, much larger than the area where high energy are found (Figure 12a), which suggests that many ions penetrate into the deep cusp but are deceleration; (iv) a striking feature is that the peak in electron energy extends to the lower edge of the SEC and connects to the high-energy peak near the possible reconnection area where Lines 30–40 extend along the poleward edge of the SEC (Figures 12b and 12d); (v) the peak width varies with altitude (Figures 12c and 12d), which allows accurate identification and characterization of the equatorward and poleward edges of the exterior cusp (note that the density gradient is much stronger on the poleward edge of the SEC and mainly extends along the plasma lobe), and (vi) the electron kinetic energy reaches a maximum value at the upper edge of the cusp (at Line~30) which is adjacent to the ATL.

A large number of ions and electrons may possibly enter the cusp mainly through the reconnection region. Electrons can enter into the cusp from both the reconnection region and exterior cusp. Ions have large gyroradii and mainly enter the cusp through the relatively small reconnection region. The difference between ion and electron 3-D gyromotions may lead to the difference between ion and electron kinetic energy distributions in Figure 12. The cause of these differences is due to complicate 3-D cusp structures in time and space and the complicate ions and electron motions in the complicate 3-D magnetosphere structure. Further investigation is required and will be discussed elsewhere.

5. Conclusions and Discussions

In the present paper, we have performed a 3-D global electromagnetic full PIC simulation of the interaction between the solar wind and the terrestrial magnetosphere under a northward IMF configuration. Within this self-consistent approach, our attention is mainly focused on the cusp region, its topology, its boundaries and the associated particles dynamics in terms of the primary macroscopic momenta, i.e., density, currents, and kinetic energies, separately for both ions and electrons.

In a first step, our PIC simulation results have been compared with the 3-D MHD simulations performed by *Wang et al.* [2004] in order to validate our results. Despite small discrepancies, our global PIC simulation shows good agreement over macroscopic scales. This encouraging comparison confirms previous agreement obtained for magnetic sash structures derived from 3-D MHD [*White et al.,* 1998] and 3-D global PIC simulations.

Despite some limitations due to computational constraints, global PIC simulations offer significant advantages over other approaches, such as hybrid and MHD simulations, in terms of (i) self-consistency in wave-particle interactions, (ii) access to separate information on electrons and ions and associated scales

(even if the mass ratio is not fully realistic), and (iii) inclusion of related kinetic effects. However, present PIC simulations also have limitations. In particular, thin boundaries layers cannot yet be reproduced; the coarse grid size and the size of the time step exclude modeling most plasma instabilities. However, kinetic effects in terms of interactions of both electrons and ions with the macroscopic E and B fields are fully included. Present simulations can reproduce the main boundary features of the terrestrial magnetosphere, such as, (i) the bow shock (leading to a strong redirection and braking of the incident solar wind), (ii) the magnetosheath, (iii) the magnetopause (identified by the last closed field line of the terrestrial dipolar field and a local pile up of the IMF), (iv) the internal ring current mainly supported by the electrons, and (v) the near cross-tail current in the night-dawn side mainly supported by the oblique ion flux.

In a second step, we have focused on analysis of the cusp region that is shown to be very active for precipitation and acceleration of solar wind particles at high latitude, i.e., a region where kinetic effects play an important role that justifies the use of PIC simulations like that shown here. Present results show that several diagnostics are necessary to accurately define the cusp and its associated boundaries and that the analysis of the magnetic field topology alone is far from being enough. In this study we have compared features of the cusp derived from the PIC simulation with those obtained from 3-D-MHD simulations and with statistical observations from the Cluster mission, performed by *Lavraud et al.* [2005] under a northward IMF configuration. Most comparisons have been performed within the meridian plane, since statistical the Cluster results are only currently available in this plane:

1. First, our PIC simulation reproduces a stagnant exterior cusp (SEC) region very similar to that found in the statistical Cluster results. This cusp region and its surroundings are characterized by the following features: (i) upward FA flows at very high altitude in the magnetosheath (above the SEC), which corresponds to a tailward convection (large black and red ellipsoid areas in Figure 10); (ii) upward FA flows, which slightly overlap with the SEC as indicated by a blue rectangle in Figure 10b and are correlated with sunward convection (blue trapezoid region in Figure 10d); and (iii) a downward FA flow at higher latitude in the middle/low cusp region below the SEC (light blue ellipsoid region). These areas are similar to those from Cluster, although the strong upward flow at the poleward edge of SEC is shifted slightly to lower altitude and higher latitude in the cusp region of PIC simulation. The PIC simulation also shows an inversion of the FA ion flux near the poleward edge of the cusp.
2. Second, the magnetosheath region, the SEC region, and the poleward edge of the cusp have been identified in the PIC simulation and compared to the statistical Cluster study. Here again, the sunward convection that may be related to lobe reconnection near the poleward edge of the cusp is shifted slightly from the SEC to middle cusp region in the PIC versus the Cluster results, possibly due to the differing conditions between the two. More precisely, present simulations show that most of the SEC region is well associated with weak V_{perpX} flow.
3. Third, high-energy ions and electrons are observed around the lower edge of the SEC and in the middle altitude cusp just below the SEC region, These energetic particles can be used to identify most of the cusp region and its outer boundaries. In particular, electron energy can be used to identify the lower part of the cusp, since they penetrate much more deeply than ions. In addition, the high-energy electron region extends from the middle cusp region to the poleward edge of the SEC and the possible reconnection region. The electron energy reaches its maximum near the ATL.
4. Fourth, one striking feature is evidence for the ATL in simulations where flow slows from super-Alfvénic (in the magnetosheath) to sub-Alfvénic (at the upper edge of the SEC). This characteristic layer is in very good agreement with Cluster statistical results and is observed for the first time—to our knowledge—in numerical simulations. Slight differences with the statistical results are found. The ATL is shifted up radially and the reconnection area is above the ATL in the PIC simulation. *Lavraud et al.* [2002, 2004, 2005] claimed that this sub-Alfvénic flow layer is a part of the plasma depletion layer (PDL) that produces the sub-Alfvénic sunward convection flow (that is the lobe reconnection flow) and finally stabilizes lobe reconnection. In this work, we have maintained a distinction between the ATL and PDL, because further detailed 3-D analysis will be needed before their relationship can be resolved. However, the current PIC simulation results identify two complementary layers forming the extended ATL that lead to the flow transition from super- to sub-Alfvénic. One layer extends into the subsolar and dayside magnetosheath where its width quickly increases as the distance increases from the upper edge of the SEC (large trapezoid on the left-hand side in Figure 11b). The other layer extends tailward and its width progressively increases as the

distance increases from the upper edge of the SEC (as illustrated by two successive narrower trapezoids on the right-hand side in Figure 11b); this second layer approaches the intrinsic X reconnection related weak magnetic field. These two layers meet at the upper edge of the SEC, at a location where the width of the ATL is the thinnest.

The slight differences observed in the relative locations of the cusp boundaries and of the internal structures between PIC simulations and Cluster statistical results reported in this study are not surprising even if only due to the differing upstream solar wind conditions (i.e., Mach regime, direction of the IMF around the exact northward configuration) and the differing methodology used in each approach to project results into a meridional plane.

PIC simulations are found to be very helpful (i) to provide complementary diagnostics for more precisely the cusp region and its associated boundaries and (ii) to pave the way for carefully analyzing the precipitation and acceleration processes of each particle species within a self-consistent 3-D approach. As illustration, to the knowledge of the authors, the main features itemized in the list above (1–4 in this section) have not been observed in previous simulations, and most of these cannot be obtained using MHD simulations.

Acknowledgments

We would like to thank the research institute of sustainable humanosphere for providing us the access to Advanced Kyoto-daigaku Denpa-kagaku Keisanki-jikken (A-KDK) supercomputers. We would like to thank Tatsuki Ogino for his valuable advices and for encouragements and one referee for the helpful and detailed comments. We address also ours thanks to Lavraud for valuable comments on our research. We also appreciate critical readings by A. Hadid and L. Krause. We, especially, thank Dennis Gallagher for his intensive reading. K.N, is supported by NASA NNX12AH06G, NNX13AP-21G, and NNX13AP14G. The source code for the model used in this study, the TRISTAN, is freely available at http://tristan-mp.wikispaces.com/. Both the data and input files necessary to reproduce the experiments with TRISTAN, are available from the authors upon request (dongscai@gmail.com). The data are archived at the Advanced Kyoto-daigaku Denpa-kagaku Keisanki-jikken (A-KDK) centers.

Yuming Wang thanks two reviewers for their assistance in evaluating this manuscript.

References

Avanov, L., V. Smirnov, J. Waite, S. Fuselier, and O. Vaisberg (2001), High-altitude magnetic reconnection in sub-Alfvénic flow: Interball Tail observations on May 29, 1996, *J. Geophys. Res.*, *106*(A12), 29,491–29,502, doi:10.1029/2000JA000460.

Birdsall, C. K., and A. B. Langdon (2004), *Plasma Physics via Computer Simulation*, CRC Press, Boca Raton, Fla.

Borovsky, J. E., M. F. Thomsen, and R. C. Elphic (1998), The driving of the plasma sheet by the solar wind, *J. Geophys. Res.*, *103*(A8), 17,617–17,639, doi:10.1029/97JA02986.

Buneman, O. (1993), TRISTAN: The 3-D, EM particle code, in *Computer Space Plasma Physics, Simulation Techniques and Software*, edited by H. Matsumoto and Y. Omura, pp. 67–84, Terra Scientific, Tokyo.

Buneman, O., R. H. Levy, and L. M. Linson (1966), Stability of crossed-field electron beams, *J. Appl. Phys.*, *37*, 3203.

Buneman, O., C. W. Barnes, J. C. Green, and D. E. Nielsen (1980), Principles and capabilities of 3-D, EM particle simulations, *J. Comput. Phys.*, *39*, 1–44.

Buneman, O., T. Neubert, and K. I. Nishikawa (1992), Solar wind-magnetosphere interaction as simulated by a 3-D EM particle code, *Plasma Sci. IEEE Trans.*, *20*(6), 810–816.

Cai, D. S., and O. Buneman (1992), Formation and stability of polarization sheaths of a cross-field beam, *Phys. Fluids B: Plasma Phys.*, *4*, 1033, doi:10.1063/1.860226.

Cai, D. S., Y. Li, T. Ichikawa, C. Xiao, and K. I. Nishikawa (2001), Visualization and criticality of three-dimensional magnetic field topology in the magnetotail, *Earth Planets Space*, *53*, 1011–1019.

Cai, D., K. Nishikawa, and B. Lembege (2006a), Magnetotail field topology in a three-dimensional global particle simulation, *Plasma Phys. Controlled Fusion*, *48*(12B), 123.

Cai, D., X. Yan, K. Ä. Nishikawa, and B. Lembege (2006b), Particle entry into the inner magnetosphere during duskward IMF *By*: Global three-dimensional electromagnetic full particle simulations, *Geophys. Res. Lett.*, *33*, L12101, doi:10.1029/2005GL023520.

Cai, D., W. Tao, X. Yan, B. Lembege, and K.-i. Nishikawa (2009), Bifurcation and hysteresis of the magnetospheric structure with a varying southward IMF: Field topology and global three-dimensional full particle simulations, *J. Geophys. Res.*, *114*, A12210, doi:10.1029/2007JA012863.

Cargill, P., B. Lavraud, C. Owen, B. Grison, M. Dunlop, N. Cornilleau-Wehrlin, C. Escoubet, G. Paschmann, T. Phan, and L. Rezeau (2005), Cluster at the magnetospheric cusps, *Space Sci. Rev.*, *118*(1–4), 321–366.

Chapman, S., and V. C. Ferraro (1930), A new theory of magnetic storms, *Nature*, *126*(3169), 129–130.

Dunlop, M. W., P. J. Cargill, T. J. Stubbs, and P. Woolliams (2000), The high-altitude cusps: HEOS 2, *J. Geophys. Res.*, *105*(A12), 27,509–27,517, doi:10.1029/2000JA900084.

Fuselier, S., S. Petrinec, and K. Trattner (2000a), Stability of the high-latitude reconnection site for steady northward IMF, *Geophys. Res. Lett.*, *27*(4), 473–476, doi:10.1029/1999GL003706.

Fuselier, S., K. Trattner, and S. Petrinec (2000b), Cusp observations of high- and low-atitude reconnection for northward interplanetary magnetic field, *J. Geophys. Res.*, *105*(A1), 253–266, doi:10.1029/1999JA900422.

Lavraud, B., M. Dunlop, T. Phan, H. Reme, J. Ä. Bosqued, I. Dandouras, J. Ä. Sauvaud, R. Lundin, M. Taylor, and P. Cargill (2002), Cluster observations of the exterior cusp and its surrounding boundaries under northward IMF, *Geophys. Res. Lett.*, *29*(20), 1995, doi:10.1029/2002GL015464.

Lavraud, B., T. Phan, M. Dunlop, M. Taylor, P. Cargill, J.-M. Bosqued, I. Dandouras, H. Reme, J.-A. Sauvaud, and C. Escoubet (2004), The exterior cusp and its boundary with the magnetosheath: Cluster multi-event analysis, *Ann. Geophys.*, *22*(8), 3039–3054.

Lavraud, B., A. Fedorov, E. Budnik, M. Thomsen, A. Grigoriev, P. Cargill, M. Dunlop, H. Reme, I. Dandouras, and A. Balogh (2005), High-altitude cusp flow dependence on IMF orientation: A 3-year Cluster statistical study, *J. Geophys. Res.*, *110*, A02209, doi:10.1029/2004JA010804.

Ogino, T., R. J. Walker, and M. Ashour-Abdalla (1992), A global magnetohydrodynamic simulation of the magnetosheath and magnetosphere when the interplanetary magnetic field is northward, *Plasma Sci. IEEE Trans.*, *20*(6), 817–828.

Palmroth, M., T. Pulkkinen, P. Janhunen, and C. Ä. Wu (2003), Stormtime energy transfer in global MHD simulation, *J. Geophys. Res. 108*(A1), 1048, doi:10.1029/2002JA009446.

Pu, Z., Q. Shi, C. Xiao, S. Fu, H. Zhang, Q. Zong, and Z. Liu (2004), Simulation studies of high-latitude magnetospheric boundary dynamics, *Sci. China Ser. E: Technol. Sci.*, *47*(4), 421–435.

Raeder, J. (1999), Modeling the magnetosphere for northward interplanetary magnetic field: Effects of electrical resistivity, *J. Geophys. Res.*, *104*(A8), 17,357–17,367, doi:10.1029/1999JA900159.

Tsyganenko, N. A. (1996), Effects of the solar wind conditions in the global magnetospheric configurations as deduced from data-based field models, in *International Conference on Substorms, Proceedings of the 3rd International Conference held in Versailles*, edited by E. J. Rolfe and B. Kaldeich, 181 pp., European Space Agency, Paris.

Wang, Y., J. Raeder, and C. Russell (2004), Plasma depletion layer: Magnetosheath flow structure and forces, *Ann. Geophys.*, *22*, 1001–1017.
White, W. W., G. L. Siscoe, G. M. Erickson, Z. Kaymaz, N. C. Maynard, K. D. Siebert, B. U. N. Sonnerup, and D. R. Weimer (1998), The magnetospheric sash and the cross-tail S, *Geophys. Res. Lett.*, *25*(10), 1605–1608, doi:10.1029/98GL50865.
Zong, Q. Ä., T. Fritz, H. Zhang, A. Korth, P. Daly, M. Dunlop, K. Ä. Glassmeier, H. Reme, and A. Balogh (2004), Triple cusps observed by Cluster—Temporal or spatial effect?, *Geophys. Res. Lett.*, *31*, L09810, doi:10.1029/2003GL019128.
Zwan, B., and R. Wolf (1976), Depletion of solar wind plasma near a planetary boundary, *J. Geophys. Res.*, *81*(10), 1636–1648, doi:10.1029/JA081i010p01636.